Letter

Periodic table for highly charged ions

Chunhai Lyu,* Christoph H. Keitel, and Zoltán Harman
Max-Planck-Institut für Kernphysik, Saupfercheckweg 1, 69117 Heidelberg, Germany

(Received 27 February 2025; revised 6 May 2025; accepted 6 December 2025; published 31 December 2025)

Mendeleev's periodic table successfully groups atomic elements according to their chemical and spectroscopic properties. However, it becomes less sufficient in describing the electronic properties of highly charged ions (HCIs) in which many of the outermost electrons are ionized. In this work, we put forward a periodic table particularly suitable for HCIs. It is constructed purely based on the successive electron occupation of relativistic orbitals. While providing a much simplified description of the level structure of highly charged isoelectronic ions—essential for laboratory and astrophysical plasma spectroscopies, such a periodic table predicts a large family of highly forbidden transitions suitable for the development of next-generation optical atomic clocks. Furthermore, we also identify universal linear Z scaling laws (Z is the nuclear charge) in the so-called "Coulomb splittings" between angular momentum multiplets along isoelectronic sequences, complementing the physics of electron-electron interactions in multielectron atomic systems.

DOI: 10.1103/bppp-53g1

Introduction. In multielectron atomic physics, the "building-up" principle [1] states that the electron would fill atomic orbitals according to their relative energies. For neutral atoms, the repulsion interaction between electrons renders the $(n+1)s, (n+1)p$ orbitals asserting energies lower than those of the nd, nf orbitals, with n being the principal quantum number and s, p, d, f corresponding to orbital angular momenta $l = 0, 1, 2, 3$, respectively. As a consequence, the electron would fill atomic orbitals according to the increasing value of $n + l$. This principle, also called Madelung-Janet rule [1], determines the ground-state electron configurations, thus the physical and chemical properties of the corresponding transition metal, lanthanoid, and actinoid elements in the conventional periodic table [2].

However, when most of the outer-shell electrons of an atom are stripped off, it becomes a highly charged ion (HCI). Though such systems are exotic, they play a key role in laboratory and astrophysical plasmas [3–5], x-ray lasers [6–8], nanolithography [9], tumor therapy [10], optical clocks [11–13], and in testing fundamental theories [14–16]. As the electrons in HCIs feel a much stronger Coulomb interaction with the nucleus, the electrons would follow the so-called Coulomb filling rule [17]: i.e., before occupying the $(n+1)$th shell, the electron will first fill all the orbitals in the nth shell.

Periodic table. Here, we show that the Coulomb filling rule renders it possible to construct a meaningful periodic table for HCIs. This allows us to gain extraordinary insight into the physics and applications of such strong-field multielectron systems. As shown in Fig. 1, in the proposed periodic table, each cell represents an isoelectronic sequence, containing tens of ions sharing the same relativistic valence-electron configuration $nl_{\pm}^{m}$ (m is the number of electrons in the corresponding relativistic orbital and the subscripts $\pm$ stand for the single-electron total angular momentum $j = l \pm 1/2$, respectively). Then, each column groups cells with the same j^m multiplet, and each row (period) collects cells with the same $nl_{\pm}$ values, where ns, np_-, and np_+ orbitals are put in the same row to save space. As both np_+ and nd_- have $j = 3/2$, and both nd_+ and nf_- have $j = 5/2$, they are grouped into the same column, respectively.

Different from the conventional periodic table where nl_- and nl_+ orbitals are treated equivalently due to strong LS couplings, in our case for HCIs with strong jj couplings, the electrons will first fill the nl_- orbital. Only after nl_- is fully occupied with $2j+1$ electrons, the remaining electron can start to fill the nl_+ orbital. Such an arrangement is straightforward as Dirac's relativistic theory [18,19] predicts a lower orbital energy for nl_- than for its nl_+ counterpart. However, to have the abovementioned filling order, the fine-structure splittings between nl_- and nl_+ shall exceed the screening energy caused by electron-electron interactions. Therefore, our periodic table is dedicated to HCIs in which the relativistic effects of valence electrons are more significant than their screening effects. The reference ion at the bottom of each cell benchmarks the lightest element at which this rule is fulfilled, thus resembles the crossing point from LS couplings to jj couplings.

This periodic table would bear significant consequences and advances for the understanding and applications of HCIs in fields ranging from atomic physics and quantum optics to plasma spectroscopy and astrophysics, and to ultraprecise clocks.

*Contact author: chunhai.lyu@mpi-hd.mpg.de

Published by the American Physical Society under the terms of the Creative Commons Attribution 4.0 International license. Further distribution of this work must maintain attribution to the author(s) and the published article's title, journal citation, and DOI. Open access publication funded by Max Planck Society.

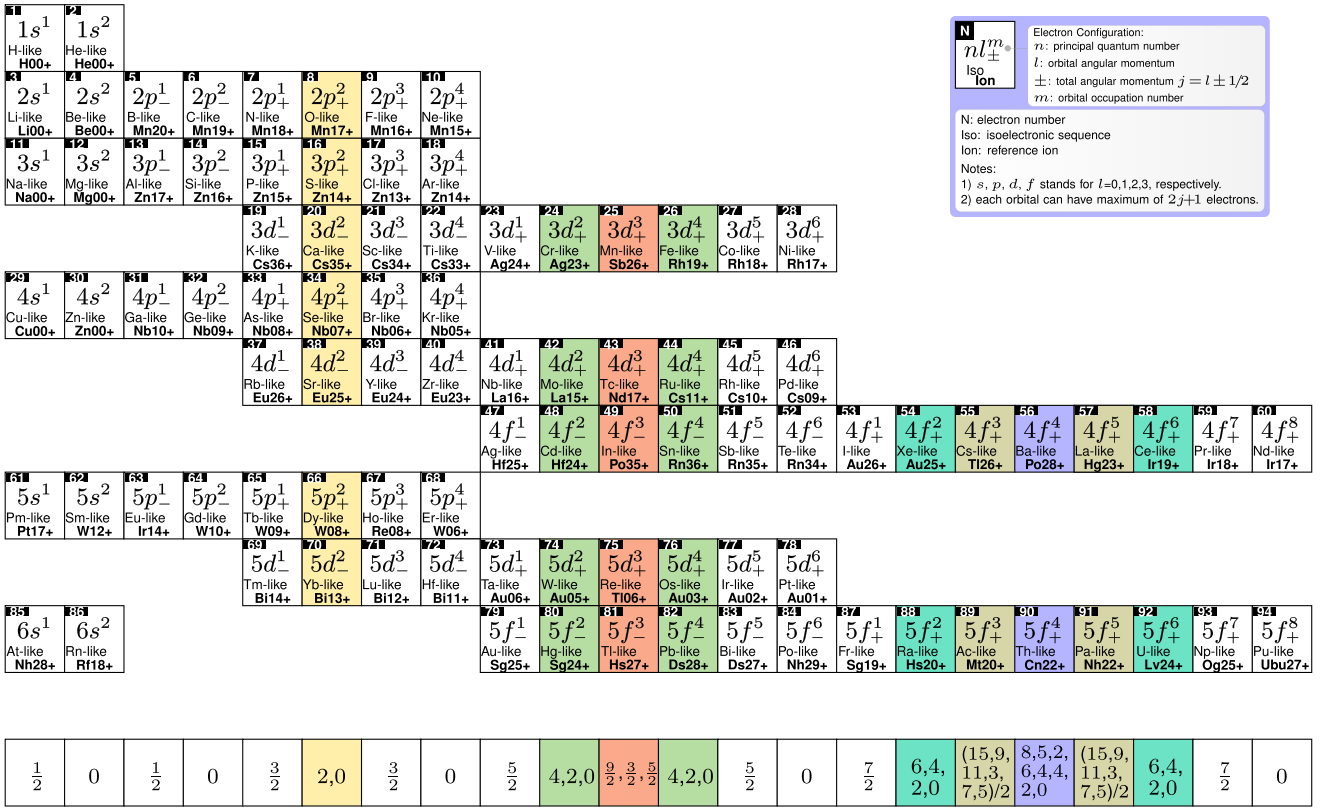


FIG. 1. Periodic table for HCIs. It is arranged according to the number of electrons N, with each cell representing one isoelectronic sequence with a given $nl^m_\pm$ configuration. The reference ions at the bottom of each cell indicate the elements in which the relativistic energy splittings between nl_- and nl_+ orbitals start to be larger than the screening energy induced by electron-electron interactions, and thus jj coupling becomes significant. As the energy of $6s$ is always lower than that of $5f_+$, the two cells with $N = 85, 86$ at the bottom-left corner of the table shall be inserted between the $5f_-^6$ ($N = 84$) and $5f_+^1$ ($N = 87$) cells. The bottom row presents all allowed J's, ordered according to their increasing energies, of the ground-state j^m multiplet in each column. This periodic table is created via LaTex by modifying the pgf-PeriodicTable package [20].

Ground states. As a first consequence, the periodic table in Fig. 1 enormously simplifies the spectroscopic analysis of complex atomic structures, and thus uncovers the periodicity of the ground states of HCIs. It is well known that atomic systems with partially filled d and f orbitals contain tremendously complicated fine-structure terms [18,21]. Without numerical calculations, it is difficult to identify their ground states [22]. However, our periodic table introduces additional closed-shell configurations, namely, the columns with fully occupied np_-^2, nd_-^4, and nf_-^6 configurations. Based on this, it allows one to define valence electron configurations and their corresponding hole states. Therefore, the ground state of HCIs can be easily identified by analyzing the angular couplings of these simplified electron configurations. The results are shown at the bottom of the periodic table in Fig. 1, where all possible multielectron total angular momenta J are listed for each column.

Take the open-shell nd^5 ions, for instance; they contain 37 fine-structure terms with $J = 1/2$ up to $13/2$ [23], and it is not obvious which term has the lowest energy. However, in our periodic table, this corresponds to an electron configuration of $[nd_-^4]nd_+^1$, with the nd_- orbital being fully occupied. The single-valence nd_+^1 electron immediately indicates that $J = 5/2$ is the only term, and thus the ground state of the corresponding HCIs. In the case of $4f^7$ ions containing 327 fine-structure states [23], the notation $[4f_-^6]4f_+^1$ directly indicates that the ground state comes with $J = 7/2$. For systems with two, three, and four valence electrons in a given $nl_\pm$ orbital, the Pauli's exclusion principle restricts the possible jj-coupling schemes, thus greatly reduces the number of states in the ground-state configurations [24]. In the bottom row of the periodic table in Fig. 1, the corresponding J's are listed in ascending order based on their energies. As expected by Hund's rule [1], the state of the highest J is the ground state. Furthermore, by sharing the same J values, it is apparent that the nd_+^1 and nd_+^2 configurations are symmetric with their hole states nd_+^5 and nd_+^4, respectively, a phenomenon that also applies to the f_- and f_+ ions.

Excited states. As a second consequence, the relativistic notation of the electronic configurations can reveal electron transitions between the l_- and l_+ subshells, and thus expose the grouped low-lying level structures of HCIs that may improve atomic plasma simulations and enable applications in x-ray quantum optics. To demonstrate this, the excited states of uranium ions from the second ($2s$, $2p_-$, and $2p_+$ ions) and the fourth ($3d_-$ and $3d_+$ ions) rows of the periodic table,

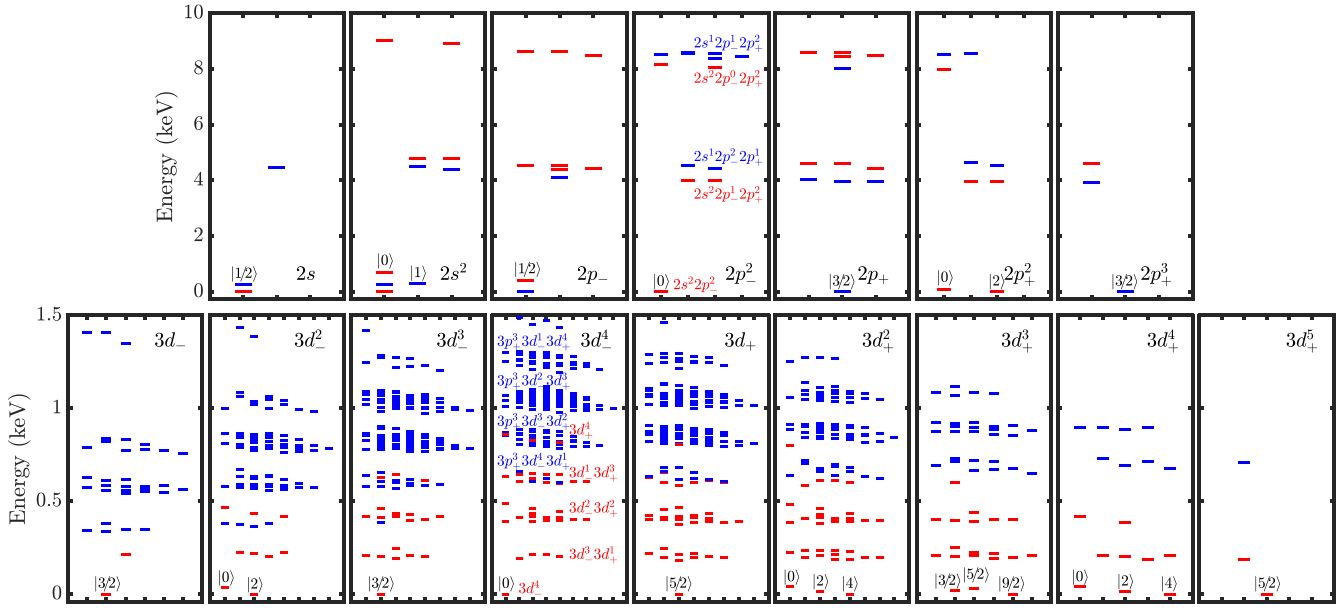


FIG. 2. Clustered level structures in highly charged uranium ions: The upper and lower panels correspond to the ions from the second and fourth rows of the periodic table shown in Fig. 1, respectively. Horizontal axis is the total angular momentum, with the first tick point being 0 (or 1/2) for integer (or half-integer) J's. The parity is colored in red (blue) for even (odd) states. In the lower panel, levels in blue color are the states formed by single excitation mainly from the $3p_+$ subshell, with the level energy around 1.4 keV being the single excitation from the $3p_-$ subshell.

calculated with the GRASP2018 codes [23], are shown in Fig. 2. From the upper panel, a distinct grouping of the $2s$ and $2p_-$ orbitals and their sequential excitations to the high-lying $2p_+$ orbitals are observed. The better proximity of the $2p_-$ to the $2s$ than the $2p_+$ orbital, resembling a screened hydrogenlike system, is a direct consequence of strong relativistic effects in HCIs.

In the lower panel of Fig. 2, the complicated fine-structure levels (red color) of each $3d_\pm^m$ ion are clustered into one-, two-, three-, and four-electron excitations from the $3d_-$ to the $3d_+$ orbital. The similarities in the level structures between the $3d_-^{4-q}3d_+^q$ and $3d_-^q3d_+^{6-q}$ excited configurations ($q \leqslant 4$ is the number of excitations) recover a particle-hole symmetry in both $3d_-$ and $3d_+$ subshells. Limited by dense, complex atomic states in multiply excited ions, state-of-the-art collisional-radiative atomic plasma models [25,26] usually employ superconfigurations [25] that mainly account for transitions between principal orbitals, to simulate ionic populations and fluorescence in plasmas. The grouped level structures observed in Fig. 2 bring forth a manageable approach to extend these models to include transitions between states based on relativistic configurations [27]. This would allow us to resolve the multielectron excitations and ionizations of relativistic subshells, and to gain insight into the astrophysical and laboratory atomic plasma processes in fields ranging from laser-produced plasma [7,8] and warm dense matter [28], to confined fusion [29–31] and to solar systems [4].

Furthermore, the lifetimes of these excited configurations, manifested by magnetic-dipole decays, are in the range of 10 ns. This corresponds to a time scale similar to that in the excited states of neutral atoms manifested by electric-dipole-allowed decay in the optical range [32,33]. Thus, the abundant low-lying Λ-, Ξ-, and V-type level structures observed in Fig. 2 are ideal experimental platforms for the development of x-ray quantum optics [34–39].

Forbidden transitions. The third consequence from this periodic table is that it predicts a large family of highly forbidden optical and XUV transitions. This may enable the construction of next-generation atomic clocks [12,40–42]. The corresponding transitions are from ions highlighted by the colored columns of the periodic table shown in Fig. 1, where the valence orbitals are multiply occupied. Due to the Pauli exclusion principle in orbital filling, the ground-state configurations of these ions contain multiple J's whose values differ from each other by 2 or 3 (see the bottom row of Fig. 1). As a result, the lifetimes of the corresponding excited states are dominated by decays via highly forbidden electric quadrupole ($E2$) or magnetic octupole ($M3$) transitions that allow for the development of ultrastable HCI clocks [11]. To be more explicit, the level structures of the $2p_+^2$, $3d_-^2$, $3d_+^2$, $3d_+^3$, and $3d_+^4$ ions can be found in Fig. 2. Within these ground-state configurations, the low-lying levels are well isolated from the states involving excitations from the l_- to the l_+ subshells. Take the $3d_+^2$ and $3d_+^4$ configurations, for example, they are the two-electron and two-hole states of the $3d_+$ orbital. Therefore, within the ground-state configurations, they share the same level structure; i.e., with $|4\rangle$ being the ground state, the $|2\rangle$ state is the first excited state whose 100–1000 s lifetime is manifested by slow $E2$ decay. Thus, the $|4\rangle \to |2\rangle$ transition in both systems can serve as an ultrastable clock reference with projected instabilities [41] $\sigma_y \sim 10^{-17}/\sqrt{\tau}$ (τ is the average measuring time).

In total, we identified more than 700 HCI clock candidates. Their key properties and their comparison with state-of-the-art clocks are presented in Fig. 3. Here, each line in the figure corresponds to one of the 24 isoelectronic sequences, ranging

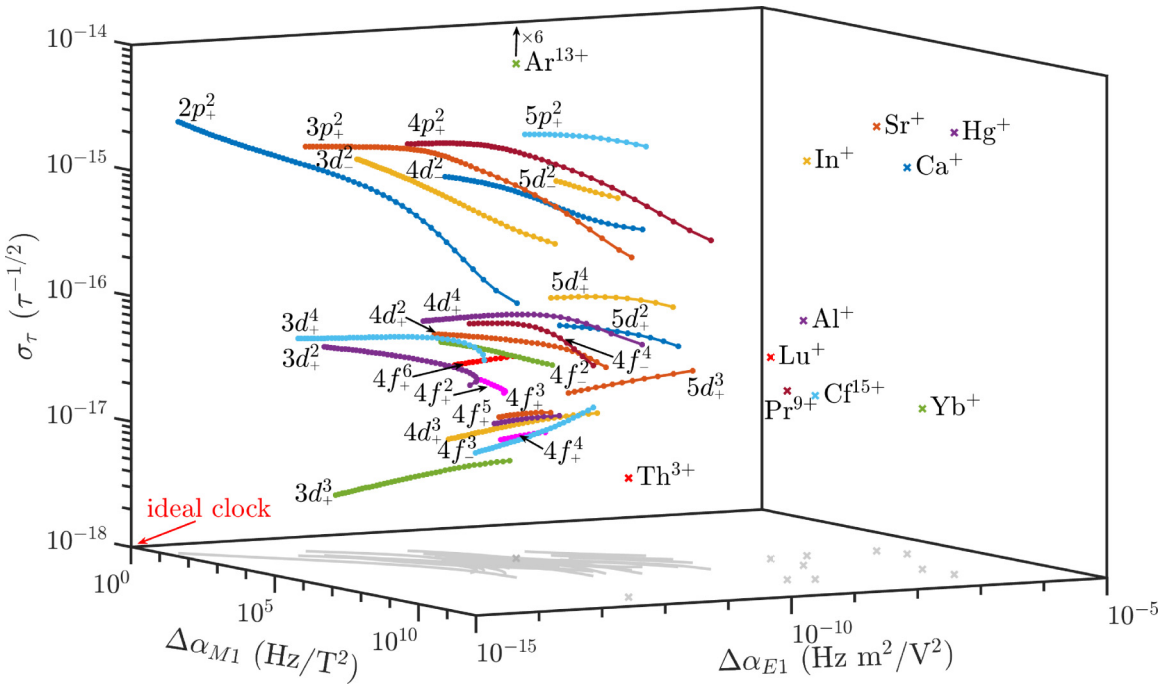


FIG. 3. Superior clock properties of HCI clock candidates. The projected instability σ_τ, and differential magnetic- ($\Delta\alpha_{M1}$) and electric-dipole ($\Delta\alpha_{E1}$) polarizability of over 700 HCI clock candidates are plotted, with the gray lines and crosses being their projections in the x–y plane. Each line corresponds to a relevant isoelectronic sequence denoted by the colored cells in the periodic table of Fig. 1. The values for state-of-the-art singly charged ion clocks [12,43], Ar^{13+} [11], Pr^{9+} [44], Cf^{15+} [45], and nuclear clock $^{229}Th^{3+}$ [46] are presented for comparison.

from $2p_+^2$ up to $5d_+^4$ (the $5f_\pm^m$ ions are not included as they are all from elements with a nuclear charge $Z > 92$). The projected instability characterizes statistical uncertainty (or precision) of the clock candidates, and the differential electric- and magnetic-dipole polarizabilities characterize the systematic shifts (or accuracies) under the perturbation of external electromagnetic fields [41]. Details can be found in Fig. S3 of the Supplemental Material [24]. In comparison to other constructed and planned clock references [12,13], as depicted by the crosses in Fig. 3, these HCI clock references are far less sensitive to perturbations of external electromagnetic fields. Therefore, they would result in blackbody radiation shifts, ac Stark shifts, and second-order Zeeman shifts, all up to 3–5 orders of magnitude smaller than those of state-of-the-art clocks [47,48], as well as the planned $^{229}Th^{3+}$ nuclear clock [49], rendering it possible to demonstrate clocks with fractional precision $\delta\nu/\nu < 10^{-20}$. High-precision spectroscopy [50] of the isotope shifts of this vast range of narrow transitions would find applications in, e.g., King-plot analysis [51–59], and thus enriching the test of nuclear theories and the search for physics beyond the standard model [60].

Coulomb splitting. The emergence of the physics discovered above can be illustrated in Fig. 4. Here, the evolution of the energies of the low-lying states, as a function of nuclear charge Z, is plotted for isoelectronic systems of nd^2, nd_+^2, nd^3, and nd_+^4 ($n = 3, 4, 5$) configurations. While these states intertwined together in the cases of light elements (i.e., small Z), it is obvious that their excitation energies evolve into two distinct scaling laws for heavy ions (i.e., large Z). For states involving electron excitations between the l_- and l_+ orbitals, their energies scale as Z^4/n^3 that feature the Z^2Z^{*2}/n^3 scaling laws for the relativistic fine-structure splittings [18,61] (Z^* is the effective charge under electron screening effect).

For states whose energies scale linearly with Z in Fig. 4, they are all from the corresponding ground-state configurations listed in the bottom row of the periodic table (Fig. 1). In the case of nd_+^2, our analytical calculation predicts (in atomic units)

$$E_2 - E_4 = \tfrac{24}{175}R_2 - \tfrac{2}{63}R_4, \tag{1}$$

$$E_0 - E_4 = \tfrac{12}{35}R_2 + \tfrac{1}{9}R_4. \tag{2}$$

Here, $E_{0,2,4}$ are the energies of the $J = 0, 2, 4$ states, respectively, with $R_k = \int dr_1 \int dr_2 \rho(r_1)\rho(r_2) r_<^k / r_>^{k+1}$ [$k = 2, 4$, and $r_> = \max(r_1, r_2)$ and $r_< = \min(r_1, r_2)$] being the Slater integral of rank k [18,61] and $\rho(r)$ the electron density of the radial wave function of the nd_+ orbital. As $R_k \propto \langle \frac{1}{r} \rangle \propto Z/n^2$ [18] is a measure of the strength of the electron-electron interactions, Eqs. (1) and (2) indicate that there is a significant cross cancellation of relativistic effects in the energy splittings between these states. Due to such a linear scaling law, as shown in Fig. 4, the energies of these states quickly become well isolated from those of the states involving interorbital excitations. As a consequence, it leads to the reordering of the fine-structure terms, and to the highly forbidden optical and XUV transitions discussed in Fig. 3. The slopes of the lines would thus directly reflect the scalings of the screening effects arising from the interactions between the valence electrons in these ions. In the periodic table of Fig. 1, the reference ions

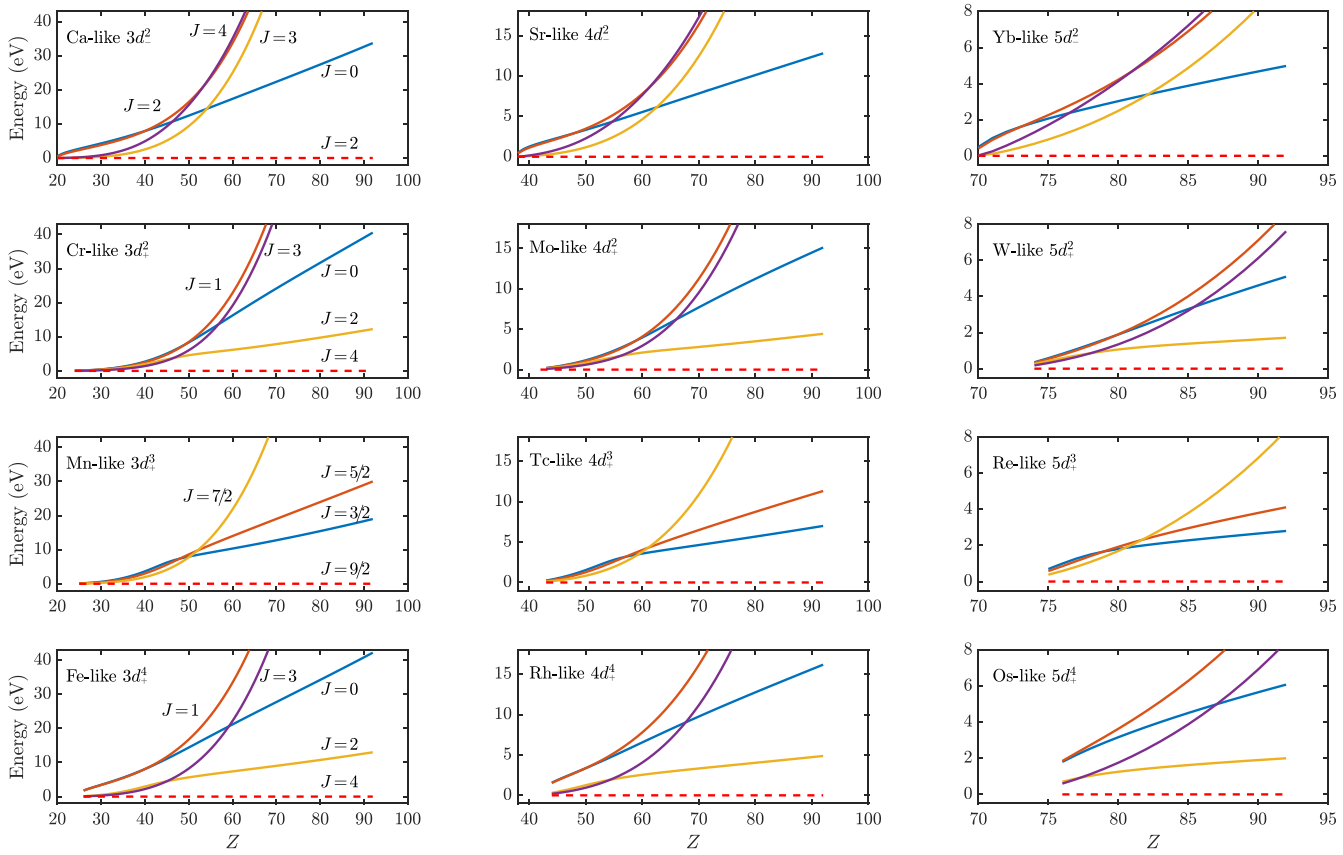


FIG. 4. Universal linear scaling laws manifested by mutual-electron interactions. Energies of the low-lying levels of the nd_-^2, nd_+^2, nd_+^3, and nd_+^4 ions are plotted as functions of the atomic number Z. The energies that scale linearly with Z are all from the ground-state multiplets listed at the bottom of the periodic table in Fig. 1.

at which the first term reordering happens are displayed at the bottom of each cell. This mechanism also explains the grouped level structures of the excited $3d_-^{4-q}3d_+^q$ configurations observed in Fig. 2.

In conclusion, our periodic table facilitates the spectroscopic analysis of the grouped level structures in complex highly charged atomic systems, which might find applications in various plasma research works. With a single, simple theory under angular momentum couplings of relativistic orbitals, we are able to discover and categorize hundreds of ultrastable HCI clock candidates, whose projected performance could surpass state-of-the-art clocks by several orders of magnitude. Furthermore, with both numerical and analytical methods, we also identify the universal Z/n^2 scaling laws in the energy splittings between states from the same relativistic configurations in HCIs. As these splittings are a consequence of the electron-electron interaction terms in the multielectron atomic Hamiltonian [18,61], the observed linear scaling laws complement the quadratic Z^2/n^2 scaling laws in principal energies governed by the central Coulomb potential of the nucleus, and the Z^4/n^3 scaling laws in fine-structure splittings manifested by the relativistic effects. To distinguish it from the well-known fine-structure splitting, we suggest to name this type of splitting "Coulomb splitting." These Z scaling laws would provide a systematic understanding of the spectroscopic properties of HCIs in various plasma conditions.

Acknowledgment. C.L. thanks Dr. Li Han and Dr. Suvam Singh for discussions and reading the manuscript.

Data availability. The data supporting this study's findings are available within the Letter.

Appendix A: Analytical methods. To obtain all the total angular momenta J for the ground-state configuration of each cell in the periodic table of Fig. 1, we employ the jj-coupling scheme based on the particle creation and annihilation operators. For two-valence-electron systems, this is [61]

$$|JM\rangle = \sum_{m_a,m_b} C_{ab}^{JM} a_a^\dagger a_b^\dagger |0\rangle. \tag{3}$$

Here, $|JM\rangle$ is the energy eigenstate with a total angular momentum J and magnetic component M, and $|0\rangle$ the vacuum state. $a_i^\dagger$ $(i = a, b)$ creates one electron in the relativistic orbital with angular momentum j_i and magnetic component m_i. $C_{ab}^{JM} = C(j_a, j_b, J; m_a, m_b, M)$, with $M = m_a + m_b$, is the corresponding Clebsch-Gordan coefficient that can be calculated via software such as Mathematica. As we are interested in the ground-state configurations, such as the np_+^2, nd_-^2, nd_+^2, nf_-^2, and nf_+^2, one always has $j_a = j_b$. After accounting for the Pauli's exclusion principle, all allowed combinations of electron occupations can be determined, and are listed in Tables S1–S4 of the Supplemental Material [24]. With similar procedures, one can also obtain the configuration state functions (CSFs) for three- and four-electron systems, namely, the nd_+^3, nf_-^3, nf_+^3, and nf_+^4 configurations.

In the following, we take the nd_+^2 and nf_-^2 configurations as an example to demonstrate the analytical considerations discussed in the main text. As shown in Table S2 of the Supplemental Material [24], there is only one occupation scheme for both $|M=4\rangle$ and $|M=3\rangle$ states. As these two Fock states will be accounted into the magnetic levels for the state with $J=4$, it means that there is no state with $J=3$ allowed in such a configuration. With similar considerations, one can also exclude the $J=1$ state. Therefore, only the states with $J=4,2,0$ are allowed in the nd_+^2 and nf_-^2 configurations. With the help of Eq. (3), the three $|M=0\rangle$ Fock states can be used to construct the corresponding three atomic states

$$|00\rangle = \sqrt{\frac{1}{3}}S_{\frac{1}{2},\frac{-1}{2}} - \sqrt{\frac{1}{3}}S_{\frac{3}{2},\frac{-3}{2}} + \sqrt{\frac{1}{3}}S_{\frac{5}{2},\frac{-5}{2}},$$

$$|20\rangle = -\sqrt{\frac{8}{21}}S_{\frac{1}{2},\frac{-1}{2}} + \sqrt{\frac{1}{42}}S_{\frac{3}{2},\frac{-3}{2}} + \sqrt{\frac{25}{42}}S_{\frac{5}{2},\frac{-5}{2}},$$

$$|40\rangle = \sqrt{\frac{2}{7}}S_{\frac{1}{2},\frac{-1}{2}} + \sqrt{\frac{9}{14}}S_{\frac{3}{2},\frac{-3}{2}} + \sqrt{\frac{1}{14}}S_{\frac{5}{2},\frac{-5}{2}},$$

with the Slater determinants being defined as

$$S_{ab} = \frac{1}{\sqrt{2}}(a_a^\dagger a_b^\dagger - a_b^\dagger a_a^\dagger)|0\rangle = \frac{1}{\sqrt{2}}(|ab\rangle - |ba\rangle).$$

With the above wave functions, one can proceed to calculate the energy of these atomic states. By defining the closed-shell core as the vacuum state, one has the energy

$$E_{JM} = 2\epsilon + \sum_{m_a m_b}\sum_{m_c m_d} C_{ab}^{JM} C_{cd}^{JM} g_{abcd},$$

with ϵ being the one-particle energy of the electron in the nd_+ or nf_- orbital, and $g_{abcd} = \langle ab|\frac{1}{r_{12}}|cd\rangle$ the two-body matrix elements describing electron-electron Coulomb interactions (in atomic units). With further mathematical derivations, it can be proved that E_{JM} is independent of the magnetic component M such that

$$E_4 = 2\epsilon + R_0 - \tfrac{4}{35}R_2 - \tfrac{1}{63}R_4, \tag{4}$$

$$E_2 = 2\epsilon + R_0 + \tfrac{4}{175}R_2 - \tfrac{1}{21}R_4, \tag{5}$$

$$E_0 = 2\epsilon + R_0 + \tfrac{8}{35}R_2 + \tfrac{2}{21}R_4. \tag{6}$$

Here, $R_k = \int dr_1 \int dr_2 \rho(r_1)\rho(r_2) r_<^k / r_>^{k+1}$ [$k = 0, 2, 4$, and $r_> = \max(r_1, r_2)$ and $r_< = \min(r_1, r_2)$] is the Slater integral of rank k [18] and $\rho(r)$ the radial electron density of the nd_+ or nf_- orbital. As R_k is always positive and $R_2 > R_4$, it is obvious that $E_4 < E_2 < E_0$. The common term $2\epsilon + R_0$ in the energies of all three CSFs indicates that the excitation energies of the $J = 2, 0$ states are mainly determined by electron-electron interactions.

Appendix B: Numerical methods. The level structures, lifetimes, and line strengths mentioned in the main text were calculated via the *ab initio* fully relativistic multiconfiguration Dirac-Hartree-Fock (MCDHF) and relativistic configuration interaction (RCI) methods implemented in the GRASP2018 code [23]. Within this approach, the many-electron atomic state function (ASF) is constructed as a linear combination of configuration state functions with common total angular momentum (J), magnetic (M), and parity (P) quantum numbers:

$$|\Gamma PJM\rangle = \sum_k c_k |\gamma_k PJM\rangle.$$

Each CSF $|\gamma_k PJM\rangle$ is built from products of one-electron orbitals (Slater determinants), jj coupled to the appropriate angular symmetry and parity, and γ_k represents orbital occupations, together with orbital and intermediate quantum numbers necessary to uniquely define the CSF. Γ collectively denotes all the γ_k involved in the representation of the ASF. c_k is the corresponding mixing coefficient. The radial wave function for each orbital is obtained via solving the self-consistent MCDHF equations under the Dirac-Coulomb Hamiltonian. Then, the RCI method is applied to account for corrections arising from mass shift, quantum electrodynamic, and Breit interactions.

As there are more than 700 HCI clock candidates, and to identify the positions of the reference ions listed in the periodic table of Fig. 1, more than 1000 ions need to be calculated. Therefore, it is time consuming to fully account for the correlation effects for all these ions. Luckily, the correlation effects may shift the excitation energies; they do not modify the conclusions discussed in the main text. Therefore, only the leading correlation effects arising from single-electron excitations from the $\{n(l-1), nl\}$ valence orbitals to all the $\{n+1\}$ correlation orbitals are included in the GRASP2018 calculations.

Appendix C: Reference ions. As there is no commonly accepted definition of highly charged ions, in this work, whether the ion is highly charged or not is based on the interplay of relativistic effects (energy splittings between l_- and l_+ orbitals) and electron-electron interactions.

In our periodic table, the reference ion is the first ion in the corresponding isoelectronic sequence in which the relativistic energy splittings between l_- and l_+ orbitals become larger than the electron-electron interactions, and thus their ground-state configuration can be properly described by the jj-coupling scheme. For example, Ca-like ions have $N = 20$ electrons. The reference ion Cs^{35+} means that the ground-state configuration of those isoelectronic ions with $Z \geqslant 55$ can be described as $3d_-^2$, with $J = 2$ being the ground state and $J = 0$ being the first excited state.

The determination of Cs^{35+} as the reference ion for Ca-like ions is based on the two scaling laws observed in Fig. 4. The Z^4 scaling in relativistic energy splittings and the Z scaling in the electron-electron interactions lead to reordering of the fine-structure terms in HCIs. Cs^{35+} is the first Ca-like ion in which the relativistic energy splitting between $3d_-$ and $3d_+$ orbitals is large enough such that the $J = 0$ state finally becomes the first excited state. For the nearby K-like ($3d_-^1$), Sc-like ($3d_-^3$), and Ti-like ($3d_-^4$) ions, as there is only one angular momentum state in the ground-state configuration, their reference ions are simply given as Cs^{36+}, Cs^{34+}, and Cs^{33+}, respectively, based on the result of Ca-like ions.

In the case of ns orbitals ($n \leqslant 4$), as there is no fine structure, the whole isoelectronic system from the neutral atom to highly charged uranium ion shares the same ground-state configuration. Therefore, the reference ions for these cells are all neutral atoms. For the case of $5s$ and $6s$, however, one has to wait until their orbital energy becomes higher than that of $4f$ and $5f$, respectively.

[1] C. J. Foot, *Atomic Physics* (Oxford University Press, Oxford, 2005).

[2] P. Schwerdtfeger, O. R. Smits, and P. Pyykkö, The periodic table and the physics that drives it, Nat. Rev. Chem. **4**, 359 (2020).

[3] P. Beiersdorfer, K. Boyce, G. Brown, H. Chen, S. Kahn, R. Kelley, M. May, R. Olson, F. Porter, C. Stahle, *et al.*, Laboratory simulation of charge exchange-produced x-ray emission from comets, Science **300**, 1558 (2003).

[4] S. Bernitt, G. V. Brown, J. K. Rudolph, R. Steinbrügge, A. Graf, M. Leutenegger, S. W. Epp, S. Eberle, K. Kubiček, V. Mäckel, *et al.*, An unexpectedly low oscillator strength as the origin of the Fe XVII emission problem, Nature (London) **492**, 225 (2012).

[5] L. Schmöger, O. Versolato, M. Schwarz, M. Kohnen, A. Windberger, B. Piest, S. Feuchtenbeiner, J. Pedregosa-Gutierrez, T. Leopold, P. Micke, *et al.*, Coulomb crystallization of highly charged ions, Science **347**, 1233 (2015).

[6] J. Zhang, A. MacPhee, J. Lin, E. Wolfrum, R. Smith, C. Danson, M. Key, C. Lewis, D. Neely, J. Nilsen, *et al.*, A saturated x-ray laser beam at 7 nanometers, Science **276**, 1097 (1997).

[7] A. Depresseux, E. Oliva, J. Gautier, F. Tissandier, J. Nejdl, M. Kozlova, G. Maynard, J. Goddet, A. Tafzi, A. Lifschitz, *et al.*, Table-top femtosecond soft-x-ray laser by collisional ionization gating, Nat. Photon. **9**, 817 (2015).

[8] C. Lyu, S. M. Cavaletto, C. H. Keitel, and Z. Harman, Narrow-band hard-x-ray lasing with highly charged ions, Sci. Rep. **10**, 9439 (2020).

[9] J. Sheil, L. Poirier, A. C. Lassise, D. J. Hemminga, S. Schouwenaars, N. Braaksma, A. Frenzel, R. Hoekstra, and O. O. Versolato, Power-law scaling relating the average charge state and kinetic energy in expanding laser-driven plasmas, Phys. Rev. Lett. **133**, 125101 (2024).

[10] D. Schardt, T. Elsässer, and D. Schulz-Ertner, Heavy-ion tumor therapy: Physical and radiobiological benefits, Rev. Mod. Phys. **82**, 383 (2010).

[11] S. A. King, L. J. Spieß, P. Micke, A. Wilzewski, T. Leopold, E. Benkler, R. Lange, N. Huntemann, A. Surzhykov, V. A. Yerokhin, *et al.*, An optical atomic clock based on a highly charged ion, Nature (London) **611**, 43 (2022).

[12] A. D. Ludlow, M. M. Boyd, J. Ye, E. Peik, and P. O. Schmidt, Optical atomic clocks, Rev. Mod. Phys. **87**, 637 (2015).

[13] M. G. Kozlov, M. S. Safronova, J. R. Crespo López-Urrutia, and P. O. Schmidt, Highly charged ions: Optical clocks and applications in fundamental physics, Rev. Mod. Phys. **90**, 045005 (2018).

[14] J. Morgner, B. Tu, C. König, T. Sailer, F. Heiße, H. Bekker, B. Sikora, C. Lyu, V. Yerokhin, Z. Harman, *et al.*, Stringent test of QED with hydrogen-like tin, Nature (London) **622**, 53 (2023).

[15] R. Loetzsch, H. F. Beyer, L. Duval, U. Spillmann, D. Banaś, P. Dergham, F. Kröger, J. Glorius, R. E. Grisenti, M. Guerra, *et al.*, Testing quantum electrodynamics in extreme fields using helium-like uranium, Nature (London) **625**, 673 (2024).

[16] J. C. Berengut, V. A. Dzuba, and V. V. Flambaum, Enhanced laboratory sensitivity to variation of the fine-structure constant using highly charged ions, Phys. Rev. Lett. **105**, 120801 (2010).

[17] S. Goudsmit and P. I. Richards, The order of electron shells in ionized atoms, Proc. Natl. Acad. Sci. USA **51**, 664 (1964).

[18] I. P. Grant, *Relativistic Quantum Theory of Atoms and Molecules: Theory and Computation* (Springer, New York, 2007).

[19] P. A. M. Dirac, *The Principles of Quantum Mechanics* (Oxford University Press, Oxford, 1981).

[20] H. Gomes, pgf-PeriodicTable—Create custom periodic tables of elements, version 2.1.1 (2024), `https://ctan.org/pkg/pgf-periodictable?lang=en`, accessed 7 July 2024.

[21] P. W. Atkins, J. De Paula, and J. Keeler, *Physical Chemistry* (Oxford University Press, Oxford, 2023).

[22] G. C. Rodrigues, P. Indelicato, J. P. Santos, P. Patté, and F. Parente, Systematic calculation of total atomic energies of ground state configurations, At. Data Nucl. Data Tables **86**, 117 (2004).

[23] C. Froese-Fischer, G. Gaigalas, P. Jönsson, and J. Bieroń, GRASP2018—A Fortran 95 version of the general relativistic atomic structure package, Comput. Phys. Commun. **237**, 184 (2019).

[24] See Supplemental Material at http://link.aps.org/supplemental/10.1103/bppp-53g1 for the description of the jj coupling of multiply occupied orbitals, the level structures of $4f^m$ uranium ions, and the 2D plots of the transition energies, instabilities, and differential $E1$ and $M1$ polarizabilities of the clock transitions.

[25] H. K. Chung, M. H. Chen, W. L. Morgan, Y. Ralchenko, and R. W. Lee, FLYCHK: Generalized population kinetics and spectral model for rapid spectroscopic analysis for all elements, High Energy Density Phys. **1**, 3 (2005).

[26] F. B. Rosmej, V. A. Astapenko, and V. S. Lisitsa, *Plasma Atomic Physics* (Springer, Cham, 2021).

[27] J. S. Kaastra, A. J. J. Raassen, J. de Plaa, and L. Gu, SPEX x-ray spectral fitting package, Zenodo (2024), doi:10.5281/zenodo.10822753.

[28] L. Mercadier, A. Benediktovitch, Š. Krušič, J. J. Kas, J. Schlappa, M. Agåker, R. Carley, G. Fazio, N. Gerasimova, Y. Y. Kim, *et al.*, Transient absorption of warm dense matter created by an x-ray free-electron laser, Nat. Phys. **20**, 1564 (2024).

[29] T. Pütterich, R. Neu, R. Dux, A. Whiteford, M. O'Mullane, and ASDEX Upgrade Team, Modelling of measured tungsten spectra from ASDEX Upgrade and predictions for ITER, Plasma Phys. Control. Fusion **50**, 085016 (2008).

[30] A. Kramida and T. Shirai, Energy levels and spectral lines of tungsten, W III through W LXXIV, At. Data Nucl. Data Tables **95**, 305 (2009).

[31] P. Beiersdorfer, Highly charged ions in magnetic fusion plasmas: Research opportunities and diagnostic necessities, J. Phys. B **48**, 144017 (2015).

[32] M. O. Scully and M. S. Zubairy, *Quantum Optics* (Cambridge University Press, Cambridge, 1997).

[33] C. Brif, R. Chakrabarti, and H. Rabitz, Control of quantum phenomena: Past, present and future, New J. Phys. **12**, 075008 (2010).

[34] B. W. Adams, C. Buth, S. M. Cavaletto, J. Evers, Z. Harman, C. H. Keitel, A. Pálffy, A. Picón, R. Röhlsberger, Y. Rostovtsev, *et al.*, X-ray quantum optics, J. Mod. Opt. **60**, 2 (2013).

[35] K. P. Heeg, A. Kaldun, C. Strohm, C. Ott, R. Subramanian, D. Lentrodt, J. Haber, H.-C. Wille, S. Goerttler, R. Rüffer, *et al.*, Coherent x-ray–optical control of nuclear excitons, Nature (London) **590**, 401 (2021).

[36] K. P. Heeg, A. Kaldun, C. Strohm, P. Reiser, C. Ott, R. Subramanian, D. Lentrodt, J. Haber, H.-C. Wille, S. Goerttler, *et al.*, Spectral narrowing of x-ray pulses for precision spectroscopy with nuclear resonances, Science **357**, 375 (2017).

[37] J. Haber, X. Kong, C. Strohm, S. Willing, J. Gollwitzer, L. Bocklage, R. Rüffer, A. Pálffy, and R. Röhlsberger, Rabi oscillations of x-ray radiation between two nuclear ensembles, Nat. Photon. **11**, 720 (2017).

[38] S. M. Cavaletto, Z. Harman, C. Ott, C. Buth, T. Pfeifer, and C. H. Keitel, Broadband high-resolution x-ray frequency combs, Nat. Photon. **8**, 520 (2014).

[39] C. Lyu, S. M. Cavaletto, C. H. Keitel, and Z. Harman, Interrogating the temporal coherence of EUV frequency combs with highly charged ions, Phys. Rev. Lett. **125**, 093201 (2020).

[40] A. Derevianko, V. A. Dzuba, and V. V. Flambaum, Highly charged ions as a basis of optical atomic clockwork of exceptional accuracy, Phys. Rev. Lett. **109**, 180801 (2012).

[41] C. Lyu, C. H. Keitel, and Z. Harman, Ultrastable and ultraaccurate clock transitions in open-shell highly charged ions, Commun. Phys. **8**, 3 (2025).

[42] K. Kromer, C. Lyu, M. Door, P. Filianin, Z. Harman, J. Herkenhoff, P. Indelicato, C. H. Keitel, D. Lange, Y. N. Novikov, C. Schweiger, S. Eliseev, and K. Blaum, Observation of a low-lying metastable electronic state in highly charged lead by penning-trap mass spectrometry, Phys. Rev. Lett. **131**, 223002 (2023).

[43] K. J. Arnold, R. Kaewuam, A. Roy, T. R. Tan, and M. D. Barrett, Blackbody radiation shift assessment for a lutetium ion clock, Nat. Commun. **9**, 1650 (2018).

[44] H. Bekker, A. Borschevsky, Z. Harman, C. H. Keitel, T. Pfeifer, P. O. Schmidt, J. R. Crespo López-Urrutia, and J. C. Berengut, Detection of the $5p-4f$ orbital crossing and its optical clock transition in Pr^{9+}, Nat. Commun. **10**, 5651 (2019).

[45] J. C. Berengut, V. A. Dzuba, V. V. Flambaum, and A. Ong, Optical transitions in highly charged californium ions with high sensitivity to variation of the fine-structure constant, Phys. Rev. Lett. **109**, 070802 (2012).

[46] K. Beloy, Trap-induced ac Zeeman shift of the thorium-229 nuclear clock frequency, Phys. Rev. Lett. **130**, 103201 (2023).

[47] T. Rosenband, D. Hume, P. Schmidt, C.-W. Chou, A. Brusch, L. Lorini, W. Oskay, R. E. Drullinger, T. M. Fortier, J. E. Stalnaker, *et al.*, Frequency ratio of Al^+ and Hg^+ single-ion optical clocks; metrology at the 17th decimal place, Science **319**, 1808 (2008).

[48] S. M. Brewer, J.-S. Chen, A. M. Hankin, E. R. Clements, C. W. Chou, D. J. Wineland, D. B. Hume, and D. R. Leibrandt, $^{27}Al^+$ quantum-logic clock with a systematic uncertainty below 10^{-18}, Phys. Rev. Lett. **123**, 033201 (2019).

[49] E. Peik and C. Tamm, Nuclear laser spectroscopy of the 3.5 eV transition in Th-229, Europhys. Lett. **61**, 181 (2003).

[50] P. O. Schmidt, T. Rosenband, C. Langer, W. M. Itano, J. C. Bergquist, and D. J. Wineland, Spectroscopy using quantum logic, Science **309**, 749 (2005).

[51] J. C. Berengut, D. Budker, C. Delaunay, V. V. Flambaum, C. Frugiuele, E. Fuchs, C. Grojean, R. Harnik, R. Ozeri, G. Perez, and Y. Soreq, Probing new long-range interactions by isotope shift spectroscopy, Phys. Rev. Lett. **120**, 091801 (2018).

[52] I. Counts, J. Hur, D. P. L. Aude Craik, H. Jeon, C. Leung, J. C. Berengut, A. Geddes, A. Kawasaki, W. Jhe, and V. Vuletić, Evidence for nonlinear isotope shift in Yb^+ search for new boson, Phys. Rev. Lett. **125**, 123002 (2020).

[53] C. Solaro, S. Meyer, K. Fisher, J. C. Berengut, E. Fuchs, and M. Drewsen, Improved isotope-shift-based bounds on bosons beyond the standard model through measurements of the $^2D_{3/2} - {}^2D_{5/2}$ interval in Ca^+, Phys. Rev. Lett. **125**, 123003 (2020).

[54] N. L. Figueroa, J. C. Berengut, V. A. Dzuba, V. V. Flambaum, D. Budker, and D. Antypas, Precision determination of isotope shifts in ytterbium and implications for new physics, Phys. Rev. Lett. **128**, 073001 (2022).

[55] J. Hur, D. P. L. Aude Craik, I. Counts, E. Knyazev, L. Caldwell, C. Leung, S. Pandey, J. C. Berengut, A. Geddes, W. Nazarewicz, P.-G. Reinhard, A. Kawasaki, H. Jeon, W. Jhe, and V. Vuletić, Evidence of two-source King plot nonlinearity in spectroscopic search for new boson, Phys. Rev. Lett. **128**, 163201 (2022).

[56] K. Ono, Y. Saito, T. Ishiyama, T. Higomoto, T. Takano, Y. Takasu, Y. Yamamoto, M. Tanaka, and Y. Takahashi, Observation of nonlinearity of generalized King plot in the search for new boson, Phys. Rev. X **12**, 021033 (2022).

[57] N.-H. Rehbehn, M. K. Rosner, J. C. Berengut, P. O. Schmidt, T. Pfeifer, M. F. Gu, and J. R. C. López-Urrutia, Narrow and ultranarrow transitions in highly charged Xe ions as probes of fifth forces, Phys. Rev. Lett. **131**, 161803 (2023).

[58] M. Door, C.-H. Yeh, M. Heinz, F. Kirk, C. Lyu, T. Miyagi, J. C. Berengut, J. Bieroń, K. Blaum, L. S. Dreissen, *et al.*, Probing new bosons and nuclear structure with ytterbium isotope shifts, Phys. Rev. Lett. **134**, 063002 (2025).

[59] A. Wilzewski, L. Huber, M. Door, J. Richter, A. Mariotti, L. Spieß, M. Wehrheim, S. Chen, S. King, P. Micke, *et al.*, Nonlinear calcium King plot constrains new bosons and nuclear properties, Phys. Rev. Lett. **134**, 233002 (2025).

[60] M. S. Safronova, D. Budker, D. DeMille, D. F. J. Kimball, A. Derevianko, and C. W. Clark, Search for new physics with atoms and molecules, Rev. Mod. Phys. **90**, 025008 (2018).

[61] W. R. Johnson, *Atomic Structure Theory* (Springer, New York, 2007).